

# Geophysical Research Letters<sup>®</sup>

## RESEARCH LETTER

10.1029/2023GL106059

### Key Points:

- We demonstrate an approach to capture the complex rupture process of an offshore moderate-sized earthquake using limited observations
- Direct  $P$  and  $S$  waves and  $Lg$  waves are used to image a spatiotemporal slip history of the  $M_w$  4.9 Offshore Jeju Island, Korea earthquake
- Results show a cascading rupture of four subevents on a fault, offering a deeper understanding of event mechanism in low-seismicity regions

### Supporting Information:

Supporting Information may be found in the online version of this article.

### Correspondence to:

Y. Kim,  
[younghkim@snu.ac.kr](mailto:younghkim@snu.ac.kr)

### Citation:

Han, S., Kim, W.-Y., Lim, H., Son, Y. O., Seo, M.-S., Park, J. Y., & Kim, Y. (2024). Resolving multi-stage rupture process of the 2021  $M_w$  4.9 Offshore Jeju Island earthquake from relative source time functions. *Geophysical Research Letters*, 51, e2023GL106059. <https://doi.org/10.1029/2023GL106059>

Received 23 AUG 2023

Accepted 14 JAN 2024

### Author Contributions:

**Conceptualization:** Sangwoo Han, Won-Young Kim

**Data curation:** Sangwoo Han

**Formal analysis:** Sangwoo Han

**Funding acquisition:** YoungHee Kim

**Investigation:** Sangwoo Han, Won-Young Kim, Hobin Lim, Young Oh Son, Min-Seong Seo, Jun Yong Park, YoungHee Kim

**Methodology:** Sangwoo Han, Won-Young Kim, YoungHee Kim

**Project administration:** YoungHee Kim

**Resources:** YoungHee Kim

**Software:** Sangwoo Han

© 2024. The Authors.

This is an open access article under the terms of the [Creative Commons Attribution-NonCommercial-NoDerivs License](#), which permits use and distribution in any medium, provided the original work is properly cited, the use is non-commercial and no modifications or adaptations are made.

## Resolving Multi-Stage Rupture Process of the 2021 $M_w$ 4.9 Offshore Jeju Island Earthquake From Relative Source Time Functions

Sangwoo Han<sup>1</sup> , Won-Young Kim<sup>2</sup> , Hobin Lim<sup>3</sup> , Young Oh Son<sup>1</sup> , Min-Seong Seo<sup>1</sup> , Jun Yong Park<sup>1</sup> , and YoungHee Kim<sup>1</sup> 

<sup>1</sup>School of Earth and Environmental Sciences, Seoul National University, Seoul, Republic of Korea, <sup>2</sup>Lamont-Doherty Earth Observatory of Columbia University, New York, NY, USA, <sup>3</sup>Earthquake Research Center, Korea Institute of Geoscience and Mineral Resources, Daejeon, Republic of Korea

**Abstract** We used local  $P$  and  $S$  waves, and regional  $Lg$  waves to investigate the  $M_w$  4.9 Offshore Jeju Island earthquake, whose records show evidence of a complex rupture. This earthquake provides a rare window to understand the seismogenesis of moderate-sized earthquakes on the southern Korea–East China Sea continental shelf. We computed the relative source time functions (RSTFs) by aligning the signals on the origin time of the main and its empirical Green's function (EGF) events, allowing us to use them as differential times of the EGF pair. We determined subevent locations using direct-wave RSTFs, and captured the rupture variability of the two large subevents using waveform inversion of stacked  $Lg$ -wave RSTFs. The first subevent rupture started by two weak nucleation phases and propagated slowly and bilaterally. Then the second subevent ruptured westward. Our analysis demonstrates that the  $Lg$ -wave train observed at regional distances is useful in investigating detailed slip history.

**Plain Language Summary** In-depth studies of small-to-moderate-sized earthquakes in offshore regions are often limited by sparse seismographic station coverage and a lack of close observations. Here, we demonstrate the effective use of local  $P$  and  $S$  waves and regional  $Lg$  waves to investigate the detailed rupture process of the 2021  $M_w$  4.9 Offshore Jeju Island, Korea earthquake.  $Lg$  wave is a guided  $S$  wave composed of a superposition of post-critical reflections in the crust. Detailed seismological analyses using  $Lg$  waves revealed that earthquake rupture processes can be spatially complex even in areas with low seismic activity. Our analysis demonstrates that the  $Lg$  wave observed at distances greater than 150 km from the epicenter alleviates the limited local station coverage and can be a very useful signal to image the detailed slip history of the earthquake. Our analysis revealed the rupture complexity of the earthquake, expressed as a cascade of four sequential ruptures consisting of two small nucleation phases and two large subevents. Such detailed knowledge of earthquake rupture evolution is critical for understanding seismogenesis in this stable continental region setting.

## 1. Introduction

Detailed rupture histories of the earthquake are prerequisites for understanding the physical processes of earthquake generation, fault strength, and state of stress. Moderate-sized earthquakes ( $M \sim 5$ ) can exhibit complex rupture processes due to their multiple subevents (e.g., López-Comino & Cesca, 2018; Meng et al., 2021; Wu et al., 2019). In a recent study, Pennington et al. (2022) compared slip distributions of moderate-sized strike-slip events in regions with low and high deformation rates and suggested that isolated high-slip regions (i.e., separated slip patches) can be prevalent in stable continental regions. Several numerical studies suggest that the intricacy of the rupture process can be developed under varying fault roughness and strength heterogeneity (e.g., Harris, 2004; Ohnaka, 1992; Ripperger et al., 2007).

The earthquake source time function, which is the temporal variation in the slip rate integrated over the fault during a rupture, provides important constraints to unravel rupture processes. The empirical Green's function (EGF) method, which effectively removes path and site effects, has been widely employed to retrieve the relative source time function (RSTF) of a large event at each station (Hartzell, 1978). For instance, López-Comino and Cesca (2018) and Wu et al. (2019) analyzed complex rupture processes of moderate-sized earthquakes by using the centroid time variation of subevents in RSTFs at various azimuths. Meng and Fan (2021) incorporated RSTF analysis to probe the relative location of the immediate foreshocks of the 2019 Ridgecrest earthquake sequence.

**Supervision:** Won-Young Kim, YoungHee Kim  
**Validation:** Sangwoo Han, Won-Young Kim, YoungHee Kim  
**Visualization:** Sangwoo Han  
**Writing – original draft:** Sangwoo Han, Won-Young Kim, YoungHee Kim  
**Writing – review & editing:** Sangwoo Han, Won-Young Kim, Hobin Lim, Young Oh Son, Min-Seong Seo, Jun Yong Park, YoungHee Kim

In light of recent studies of large earthquakes that uncovered overlooked tsunami potential from a hidden subevent (e.g., Jia et al., 2022), and appreciation of greatly increased seismic hazard due to cascades of large earthquakes during the 2023 Turkey earthquake (Jia et al., 2023), we analyze the detailed rupture process of the 2021  $M_w$  4.9 Offshore Jeju Island earthquake. The  $P$  and  $S$  waves from the earthquake show complex waveforms that exhibit two distinct large source pulses with a time separation of  $\sim 0.8$  s. These source pulses are preceded by two small signals that are clearly discernible on local records (Figure 1c and Figure S1 in Supporting Information S1), which can be nucleation phases that initiated the mainshock rupture (e.g., Ellsworth & Beroza, 1995, 1998). The earthquake was a vertical strike-slip faulting at a depth of  $\sim 12$  km, and the fault strikes east-west ( $275^\circ$ ) (Kim et al., 2022). The earthquake occurred in an intraplate region with low seismicity with the occurrence of small earthquakes (usually  $M < 4$ ), and hence, it provides a rare window to understand the seismogenesis of moderate-sized earthquakes in the vast continental shelf region of northeastern Asia. The offshore environment of the study region imposed challenges to analyze the source in detail. The earthquake is recorded by only a half dozen local stations with limited azimuthal coverage (Figure 1).

In this study, we retrieved RSTFs of the  $M_w$  4.9 Jeju Island earthquake to capture a detailed rupture process of subevents on the fault plane despite the limited station coverage for this offshore event. By utilizing local  $P$  and  $S$  wave, we retrieved quality RSTFs by aligning the signals at the origin time of the mainshock and the EGF event during deconvolution. These local RSTFs revealed two nucleation phases and two large amplitude subevents constituting the mainshock rupture. Back-projection of the local  $P$ - and  $S$ -wave RSTFs and 1-D source inversion of the regional  $Lg$ -wave RSTFs showed the detailed spatiotemporal extent of the rupture and variability in rupture behavior for the two large subevents. Such a complex rupture, imaged as two segmented slip patches on the fault cascading sequentially, implies heterogeneous fault frictional properties, which may commonly appear in immature faults in low-deformation regions (e.g., Pennington et al., 2022).

## 2. EGF Analysis With Local $P$ - and $S$ -Wave Observations

### 2.1. Local $P$ - and $S$ -Wave RSTFs

We employed the EGF method to retrieve the RSTFs at stations situated at local distances ( $\Delta < 100$  km) (Figure 1a). The largest aftershock of  $M_w$  2.9 is the best EGF event among aftershocks, and its  $P$ -wave first motions at common stations with mainshock are all consistent, indicating a common focal mechanism (Kim et al., 2022).  $P$  wave on the vertical and  $S$  wave on the transverse records at nine stations, mostly broadband, on the island were filtered (0.8–8 Hz) and windowed 0.5 s before and 3 s after the phase arrivals. We used the projected Landweber deconvolution (PLD) with the constraints of positivity and causality, which allowed us to define precisely the start and end times of each source pulse (Bertero et al., 1997). Before deconvolution, we ensured that four subevents share a common focal mechanism because the polarities and signal shapes of the four subevents are consistent on each observed record at all stations (see Figure S1 in Supporting Information S1).

The local RSTFs were obtained by aligning the waveforms of the EGF and the target event in the same time window starting from the origin times of each event (Text S1 and Figure S2 in Supporting Information S1). We may call these sets of RSTFs as the origin-time preserved RSTFs. In this case, the origin time differences between the target event and EGF are equally canceled out at every station; thus, a travel time difference can be represented as an offset time in the RSTF (Texts S1 and S2, Figure S2 in Supporting Information S1). This offset time was then used to determine the relative locations of the target subevents against the EGF location as the reference point of the coordinate. As shown in Figure S3 in Supporting Information S1, time alignment has minimal influence on the shape of the RSTF when a waveform window encompasses the signals of the two events. The causality constraint of PLD is adjusted such that the RSTFs involve two small subevents (Text S3 in Supporting Information S1). The RSTFs calculated with local records reveal two small nucleation events (N1 and N2) during initial  $\sim 0.2$  s and two large subevents of similar amplitudes (S1 and S2), which have a time interval of 0.6–0.9 s between the onsets with the shortest time at CJD ( $AZ = 6^\circ$ ) (Figures 1c and 1d).

### 2.2. Location of Subevents Relative to EGF Using Local RSTFs

Based on the variation in the starting time of the source pulses in the RSTF, we determined the locations of four subevents: N1, N2, S1, and S2, relative to the  $M_w$  2.9 aftershock (EGF). For N1 and N2, the peak times instead of the start times were used because of their small amplitudes (Figures 1c and 1d); namely, the hypocenters of S1 and

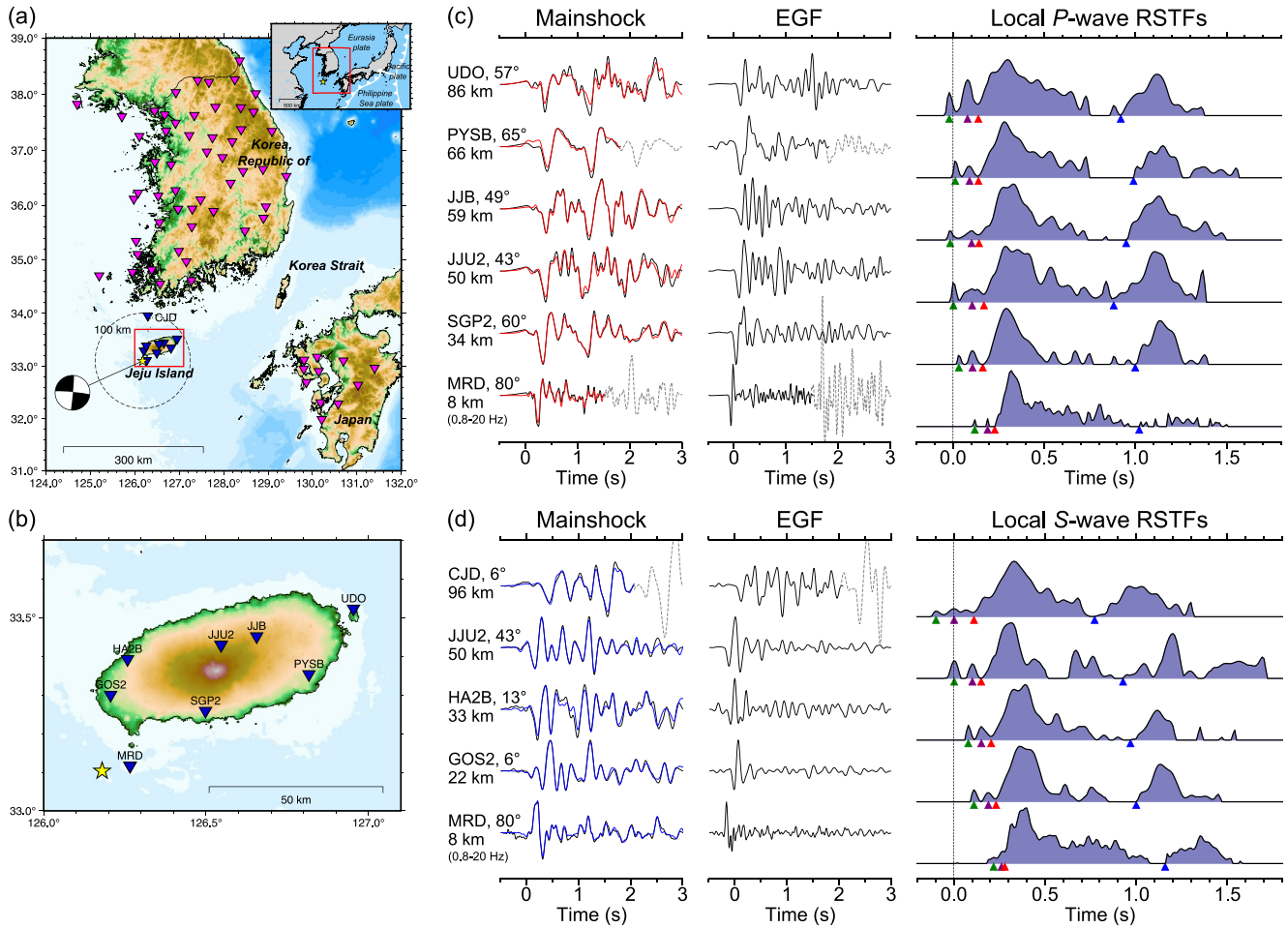


**Figure 1.** (a) Seismographic stations (inverted triangles) and  $M_w$  4.9 Offshore Jeju Island earthquake (yellow star with focal mechanism). The inset shows the tectonic framework of the study region. (b) Seismic stations at local distances (<100 km) on Jeju Island. (c) Vertical  $P$  waves from the mainshock at local stations (left column),  $P$  waves from the empirical Green's function (EGF) event (middle), and corresponding relative source time functions (RSTFs) (right). Relative source time function traces are plotted on an expanded time axis. (d) Same plot arrangement as (c) but for transverse  $S$  waves.  $P$  and  $S$  waveforms of the mainshock are compared with synthetics (red and blue traces, respectively) computed by convolving EGF and RSTFs. Synthetic traces are plotted only up to the duration of the target traces. Shorter  $P$  or  $S$  windows are used at some stations due to phase interference. Start times of subevents N1, N2, S1, and S2 are indicated as green, purple, red, and blue triangles.

S2 and the centroids of N1 and N2 were determined. The locations were grid-searched on the fault plane using least-squares minimization of the apparent time of each subevent, using the following equation:

$$\tau_i(\theta_{ij}) = \Delta t_i - \frac{D_i \cos(\theta_{ij})}{V_{P,S}} \quad (1)$$

where  $\tau_i(\theta_{ij})$  is the apparent time of the  $i$ th candidate location of subevent at the  $j$ th station measured on RSTFs,  $\theta_{ij}$  is the angle between the ray takeoff direction of the  $j$ th station and the  $i$ th candidate location vector from the EGF (Figure S2a in Supporting Information S1),  $\Delta t_i$  is the delay of the subevent origin time,  $D_i$  is the distance of the  $i$ th candidate location from the EGF, and  $V_{P,S}$  is the  $P$ - or  $S$ -wave velocities at the source depth, respectively. We used a 32 km thick two-layer crust with a 2 km thick surface low-velocity layer to calculate the ray takeoff angle at the source and for event location (Kim et al., 2022).

The relative location of each subevent on the fault plane was resolved with an average location uncertainty of less than 150 m, despite the limited station azimuthal coverage (Table S1 in Supporting Information S1 and Figure 2a). Two small subevents, N1 and N2, successively occurred at 350 m deeper depth than S1 during the first 0.2 s before the rupture of S1. S2 ruptured 0.7 s after S1 and initiated at  $\sim 0.7$  km west of S1 (Figure 2a).

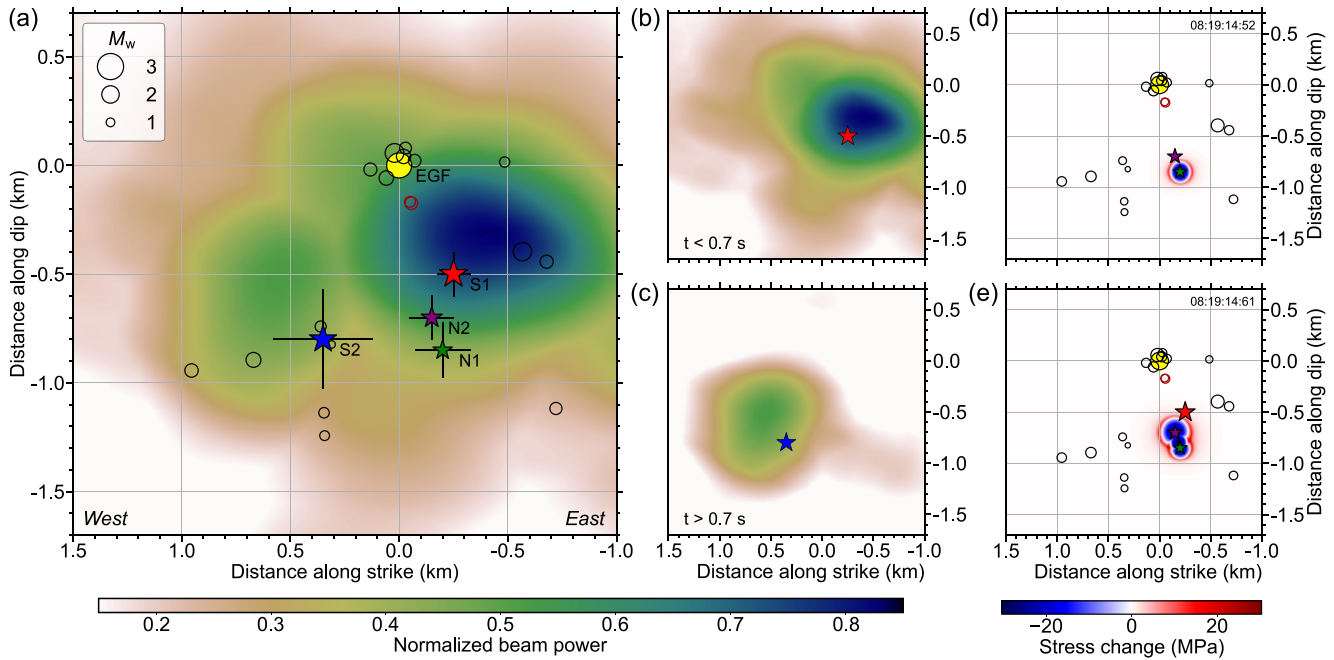


**Figure 2.** (a) Locations of nucleation events N1 and N2, and subevents S1 and S2 on the mainshock fault plane relative to the empirical Green's function event (yellow circle). Horizontal and vertical bars indicate their uncertainties (25% misfit) along strike and dip directions. Aftershocks (black circle) and foreshocks (brown circle) are shown (Kim et al., 2022). The maximum beam power obtained from the back-projection of local relative source time functions is shown in the background. Two large subevents, S1 and S2, coincide with the bright spots (shown as darker color). (b) Back-projection results at time less than 0.7 s, (c) Time greater than 0.7 s. (d) Stress changes on the fault plane by nucleation event N1 at its origin time, (e) stress change by N2, ready to exert stress to trigger subevent S1 (red star).

### 2.3. Back-Projection and Stress Perturbation Analysis

We employed back-projection using local RSTFs to track the position of high seismic energy release over time on the rupture plane (e.g., Király-Proag et al., 2019; Stabile et al., 2012).  $P$ -wave RSTF at the MRD station was not used due to its poorly defined S2 (Figure 1c). We stacked the RSTFs based on the following equation, which uses the time delay for each location on the fault plane  $\left(\frac{D_i \cos(\theta_{ij})}{V_{P,S}}\right)$  from Equation (1):

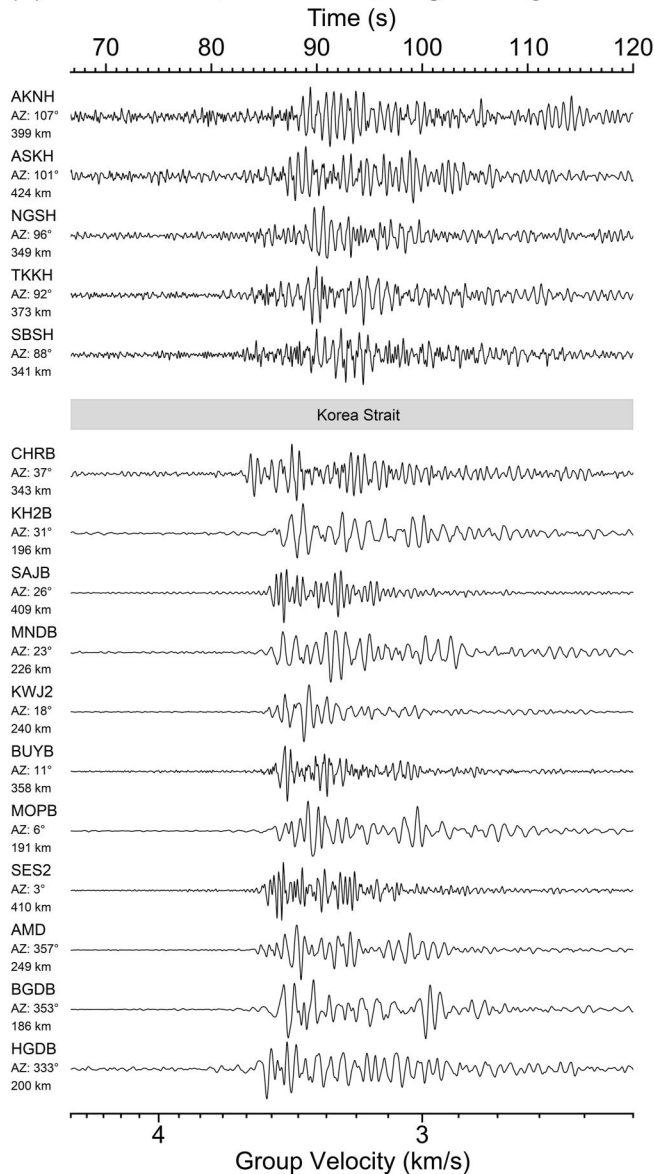
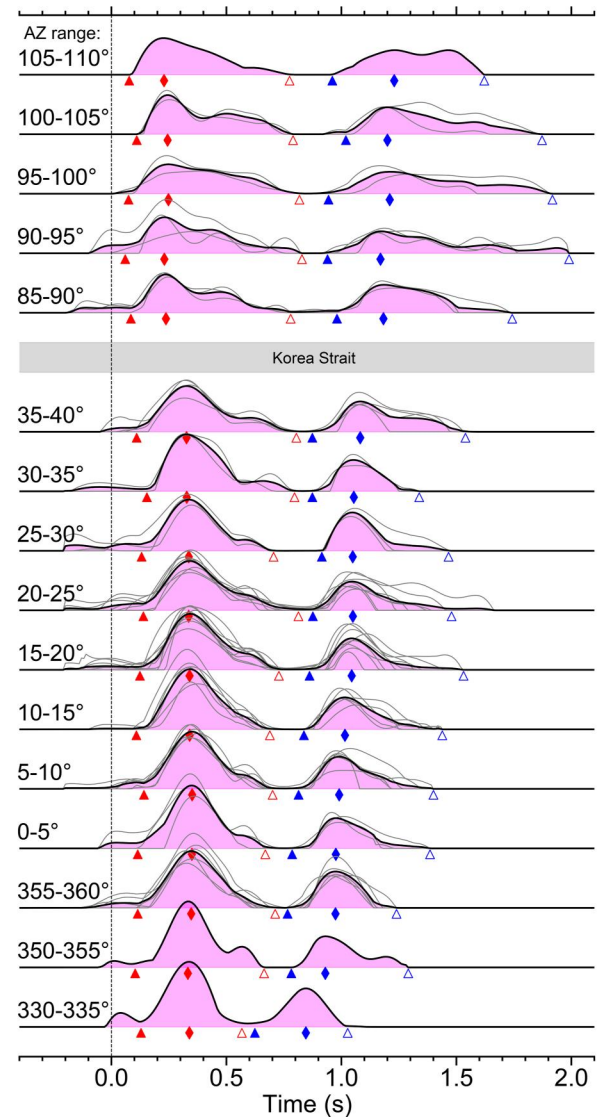
$$b_i(t) = \frac{1}{N} \sum_{j=1}^N \frac{1}{A_j} \text{RSTF}_j \left( t - \frac{D_i \cos(\theta_{ij})}{V_{P,S}} \right) \quad (2)$$

where  $b_i(t)$  is the normalized linear stacked beam power of the RSTF at  $i$ th grid point on the fault,  $N$  is the number of RSTFs ( $N = 10$ ),  $\text{RSTF}_j(t)$  is the  $j$ th index of  $P$ - or  $S$ -wave RSTF and  $A_j$  is the normalizing factor of  $\text{RSTF}_j(t)$ . The travel time or polarity correction for each station is automatically canceled out during the deconvolution process using the EGF. We used the phase-weighted stacking method with an order of 10 smoothed by 0.05 s window to achieve improved spatial resolutions (e.g., Schimmel & Paulssen, 1997).

The maximum beam power over time at each grid point on the fault plane shows two distinct bright spots (Figure 2a), which indicate the ruptured area for subevents S1 and S2 with a maximum at 0.3 and 1.0 s, respectively (Figures 2b and 2c, and Figure S4 in Supporting Information S1). The rupture area of S1 coincides with the zone of highest seismic radiation centered by its hypocenter. The rupture area of S2 extends westward from its hypocenter. Aftershocks are distributed around the periphery of bright spots, often observed in foreshock-mainshock-aftershock sequences (e.g., Kim et al., 2010).

We estimated stress changes on the fault plane induced by the nucleation events N1 and N2 in an attempt to reveal the rupture nucleation and subsequent progression (e.g., Ellsworth & Bulut, 2018) (Texts S4 and S5 in Supporting Information S1). N1 with a rupture duration of  $\sim 0.1$  s yielded a rupture of  $\sim 0.12$  km radius and stress drop of  $\sim 27$  MPa (Figure 2d). Then, N2  $\sim 0.15$  km shallower depth, just off the N1, is triggered. Assuming the self-similar rupture at constant stress drop for nucleation events (Beroza & Ellsworth, 1996), we have a source radius of  $\sim 0.16$  km for N2. N2 immediately triggered the largest subevent, S1 (Figure 2e).



(a) 2021-12-14, 08:19:15.4, Regional  $L_g$  waves

(b) Stacked regional  $L_g$ -wave RSTFs


**Figure 3.** (a) Observed  $L_g$  waves on transverse component at distances of 186–424 km plotted according to the station azimuth 333°–107°. Displacement records in the frequency band of 0.8–6 Hz are plotted on the apparent group velocity axis of 4.5–2.5 km/s. The reference time axis on top corresponds to the mean distance of 300 km starting from the event origin time. 16 out of 60 records from each of the 5°-azimuthal bins are shown. (b)  $L_g$ -wave relative source time functions (RSTFs) stacked in a 5°-azimuth bin. Individual RSTF traces in each bin are indicated as thin gray lines. The start and end times of subevents S1 (red) and S2 (blue) are represented by filled and open triangles, respectively. Diamonds indicate the peak times.

### 3. EGF Analysis With Regional $L_g$ -Wave Train

#### 3.1. Regional $L_g$ -Wave RSTFs

In addition to direct  $P$ - and  $S$ -wave RSTFs that show the location of four cascading subevents on the mainshock fault plane, we seek a method to reveal the detailed rupture process by using waveform data from densely distributed stations in the Korean Peninsula and western Japan, covering an azimuth range from  $-27^\circ$  ( $333^\circ$ ) to  $107^\circ$  (Figure 1a). For data from stations at regional distances ( $\Delta > 150$  km),  $L_g$  waves are the most prominent signals consisting of  $S$  waves multiply reflected within continental crust with mostly near-horizontal takeoff angles (Figure 3a; e.g., Campillo et al., 1984; Kim, 1987).

We calculated the RSTFs using *Lg* wave on transverse-component records filtered at a frequency band of 0.8–6 Hz, using the same PLD method used for the local RSTFs. We used data from 49 broadband stations on the Korean Peninsula ( $\Delta = 165$ –641 km) and 11 short-period stations in western Japan ( $\Delta = 339$ –488 km) (Figure 1a). Azimuthal gap of  $48^\circ$  is due to the strait between southern Korea and western Japan (the Korea Strait). *Lg* wave in the time window of 3 s before and 12 s after its arrival, with an apparent group velocity of 3.5 km/s, was used for the analysis. The time window included *Lg* signals arriving at apparent group velocity between 3.6 km/s and 3.1 km/s (Figure 3a). The RSTFs were stacked in a  $5^\circ$ -azimuth bin to enhance the robustness of their shapes (Figure 3b). The peak times for the subevents in the RSTFs in each azimuth bin were nearly constant at regional distances (Figure S5 in Supporting Information S1). Subevents S1 and S2 were observed at all stations with a short quiescence of no moment release between the two subevents, whereas the preceding small subevents were hardly discernible, probably because of high-frequency attenuation at a regional distance (Figure 3b).

### 3.2. 1-D Fault Slip Inversion

We inverted the *Lg* RSTFs to determine the spatiotemporal distribution of the fault slip on the rupture plane. We construct a 1-D line source model for the inversion modeled by  $N$  point sources along the fault strike direction of  $275^\circ$  ( $x_i$ ,  $i = 1, 2, \dots, N$ ) with an interval of 50 m (e.g., Stich et al., 2020). Slip inversion was performed with a fixed velocity of the rupture front starting from the hypocenters of S1 and S2 under the assumption that slip can only occur at the rupture front (i.e., pulse-like rupture), as shown in the following equation:

$$\text{RSTF}_j(t) = \sum_i^N A(x_i) s\left(t - t_i + \frac{x_i \cos(\varphi_j)}{V_S}, t_r\right) \quad (3)$$

where  $\text{RSTF}_j(t)$  is the  $j$ th stacked *Lg*-wave RSTF;  $A(x_i)$  is the amplitude of the slip rate being solved in the inversion;  $s(t, t_r)$  is the slip rate function at each point source, which is assumed to be a Gaussian-shaped pulse, where  $t_r$  is the risetime (defined as the duration of the seismic source emission from a point source along the fault) of each subfault, and  $\varphi_j$  is the angle between the rupture direction and the  $j$ th azimuth bin. In this case, the rupture time  $t_i$  at location  $x_i$  is defined as  $t_i = t_0 + \frac{|x_i - x_0|}{V_R}$ , where  $t_0$  and  $x_0$  are the origin time and horizontal hypocenter location of the subevent, respectively, and  $V_R$  is the rupture velocity. By using the start time of each subevent in regional *Lg* RSTFs (Figure 3b), the hypocenter location relative to the EGF event and delayed origin time are estimated as  $-100$  m (east) and 0.12 s for S1 and 600 m (west) and 0.80 s for S2, respectively (Text S6 in Supporting Information S1).

The inversion was performed independently for S1 and S2 after normalization to their moments (Text S4 in Supporting Information S1) by non-negative least-squares minimization while searching for the optimal rupture velocity  $V_R$  and risetime  $t_r$  that maximizes the variance reduction (Lawson & Hanson, 1974; Figure S6 in Supporting Information S1). The results show that S2 has  $\sim 30\%$  faster rupture velocity than S1 with similar risetime, which corresponds to the relatively larger variability of source duration of S2 (Figure S7a in Supporting Information S1). If we estimate the rupture velocity with the fixed risetime of 0.11 s, which shows the minimum misfit in both ruptures, the rupture velocities of S1 and S2 become  $1.87 \pm 0.31$  km/s ( $\sim 0.55 \times V_S$ ) and  $2.38 \pm 0.54$  km/s ( $\sim 0.70 \times V_S$ ) (uncertainty range estimated at  $1.1 \times$  optimum misfit), respectively. However, the exact value of risetime cannot be determined because of a tradeoff between rupture velocity and risetime, particularly in data over a limited azimuth range (e.g., Dreger et al., 2007).

We obtained a bimodal shape for the moment rate function by combining the inversion results for S1 and S2 (Figure 4a, inset). The rupture of S1 and S2 each lasted for  $\sim 0.5$  s with  $\sim 0.2$  s between the two subevents with zero moment release. In particular, the slip distribution indicated that the mainshock ruptured at the hypocenter of S1 and propagated east for 500 m and west for 700 m (Figure 4a, lower right). The S1 rupture can be considered an asymmetric bilateral rupture. The S2 rupture started at the western edge of the S1 rupture and propagated unilaterally westward for 650 m (Figure 4a, upper left).

Synthetic RSTFs calculated by forward modeling of the moment release at each point source were compared with the observations (Figure S8 in Supporting Information S1). The RSTFs in S2 were well-represented by the westward rupture alone, whereas in S1, the eastward rupture accounted for a non-negligible portion of the total moment release of 33% (Figure S8 in Supporting Information S1). The eastern rupture component of the bilateral

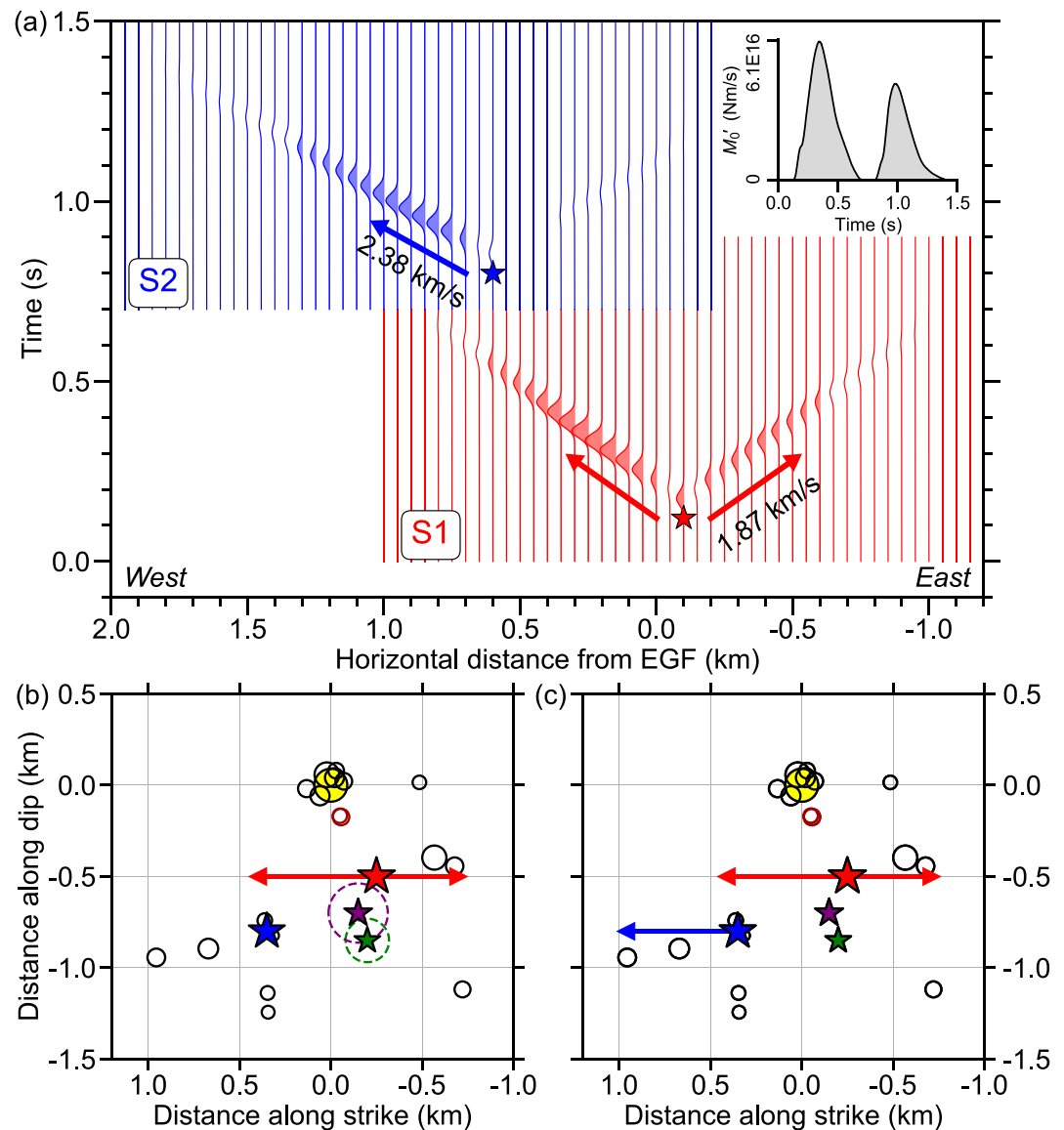


**Figure 4.** (a) Linear 1-D fault slip inversion for subevents S1 (red) and S2 (blue) using  $L_g$ -wave relative source time functions. Slip rate function of each point source at 50 m intervals is plotted with its amplitude scaled to seismic moment and colored (for relative area >1% total moment). Stars indicate the start positions of each subevent. The inset shows the source time function with two distinct peaks for the S1 and S2 ruptures. (b) Sketch of the bilateral S1 rupture. Red arrows denote the direction and length of the 1D rupture. Dashed circles are circular ruptures of the nucleation events, N1 (green) and N2 (purple). (c) Unilateral S2 rupture propagating to the west (blue arrow) is added.

rupture S1 could not be measured directly using the duration of the RSTFs observed at a limited azimuth (Figure S7a in Supporting Information S1), but it was resolvable through  $L_g$ -wave RSTFs because of its impulsive shape at stations in the east (Figure 3b), which appeared as a short time-to-peak when compared to S2 (Figure S7b in Supporting Information S1).

#### 4. Discussion

We demonstrate that by preserving the travel time difference between the main and EGF events during deconvolution, we effectively reduce possible errors during the alignment of waveforms and incorporate various phases ( $P$ ,  $S$ , and  $L_g$  waves) when retrieving RSTFs (Text S2 in Supporting Information S1). Direct  $P$  or  $S$  wave at local distances has a single takeoff angle. The RSTFs of the local  $P$  and  $S$  waves at the same azimuth can have different

start times of subevents depending on the takeoff angle. By contrast, the *Lg* wave consists of multiple reflections that were radiated with a range of takeoff angles at the source. *Lg* wave RSTFs are derived from averaging multiple reflections, yet they preserved the source properties with a smoothed effect of takeoff angles. An example of the difference between the RSTFs from the direct *P* and *S* and *Lg* waves in a narrow range of azimuth ( $0^{\circ}$ – $10^{\circ}$ ) is shown in Figure S5 in Supporting Information S1. The *S*-wave RSTF at 22 km (GOS2) has a later peak, whereas that at 96 km (CJD) has an earlier peak in terms of the vertical guiding lines, which is the mean peak time of the *Lg* RSTFs. This temporal order of peak times is due to the different takeoff angles for GOS2 and CJD, which were  $118^{\circ}$  (upgoing) and  $64^{\circ}$  (down-going), respectively. The peak times of the *Lg* RSTF are relatively constant, which implies that the RSTFs from *Lg* waves at similar azimuths can be stacked by exploiting the coherency of their waveforms (Figure 3b).

*Lg* wave has been used in EGF analysis to constrain the source spectrum corner frequency (e.g., Shi et al., 1996) and to obtain source time function from multichannel deconvolution (e.g., Gallegos & Xie, 2020). We note that the effect of *Lg* dispersion on RSTFs has been assessed (Text S7, Figures S9 and S10 in Supporting Information S1). We found that the dispersion effect is negligible, except up to  $\sim 2.1\%$  error of absolute area of RSTF may be expected along rupture direction (Figure S10 in Supporting Information S1). We demonstrated that *Lg* RSTFs are useful for constraining rupture velocity, directivity, and length (Figure 4a). *Lg* RSTFs can be effectively used by azimuthal stacking in low seismicity regions with no multiple EGF pairs available. It can be an alternative strategy of averaging RSTFs from multiple EGF pairs to improve the reliability of RSTFs (e.g., Abercrombie, 2015; Wu et al., 2019).

Based on our analysis of RSTFs, the rupture process of the  $M_w$  4.9 Jeju earthquake appears to have occurred in two stages. In the first stage, two nucleation phases occurred due to local dynamic instabilities during the mainshock nucleation (e.g., Ohnaka, 1992). These nucleation events started at deeper depths and perturbed the stress field to induce the large S1 rupture that propagated bilaterally from the nucleation point (Figure 4b). In the second stage, there is a temporal gap of  $\sim 0.2$  s before the initiation of the second large S2 subevent, implying a cascading rupture as separate slip patches on the fault (Figure 4c). Because the stress is increased at the edge of the rupture area (e.g., Andrews, 1980), a secondary rupture is triggered immediately adjacent to the primary rupture area. Slip patches with a considerable rupture velocity variability of  $\sim 30\%$  can be associated with the initial fault strength and stress state (e.g., Harris, 2004; Ripperger et al., 2007).

## 5. Conclusions

We constrained the rupture process of a moderate-sized earthquake in a stable continental region setting employing the empirical Green's function approach, revealing spatiotemporally distributed multiple subevents. Our analysis of the  $M_w$  4.9 Offshore Jeju Island earthquake shows that its rupture initiated with two nucleation phases triggering the two large subevents. The rupture velocity variation of the subevents indicates a heterogeneous initial stress and strength state of two adjacent slip patches separated by a temporal quiescence of 0.2 s. This study highlights the effective use of regional *Lg* waves to analyze the complex rupture of a moderate-sized offshore earthquake. This has a broader impact on the analysis of numerous moderate-sized offshore events occurring globally with a lack of near-source observations. Our source characterization of a moderate-sized earthquake with four cascading subevents has an important implication for evaluating seismic hazards because the ground motion amplitude is strongly influenced by rupture directivity.

## Data Availability Statement

Waveform data of the Korea Meteorological Administration were downloaded from the National Earthquake Comprehensive Information System website (<https://necis.kma.go.kr>) upon registration; data from station MRD, operated by the Korea Institute of Geoscience and Mineral Resources (KIGAM), is accessible from Geo Big Data Open Platform of KIGAM (<https://data.kigam.re.kr/quake/data/event-data>) upon registration; data from Hi-net array, operated by National Research Institute for Earth Science and Disaster Prevention (NIED) in Japan, were obtained by Python library HinetPy 0.6.8 (Tian & Kriegerowski, 2021) upon registration. We used Seismic Analysis Code version 101.6a (Goldstein & Snoke, 2005) (<https://ds.iris.edu/ds/nodes/dmc/software/downloads/sac/>) and ObsPy version 1.3.0 (<https://docs.obspy.org/>) (The ObsPy Development Team, 2022) for data processing. Figures were created using Matplotlib version 3.3.2 (<https://matplotlib.org/>) (Caswell et al., 2020);



Hunter, 2007) to support transparency. Maps were created through PyGMT version 0.7.0 (<https://www.pygmt.org/>) (Uieda et al., 2022), a Python library based on Generic Mapping Tools version 6 (<https://www.generic-mapping-tools.org/>) (Wessel et al., 2019).

## Acknowledgments

This study was supported by the Brain Pool Program of the National Research Foundation (NRF) of Korea (Grant 2020H1D3A2A02047949). S. Han, Y. O. Son, M.-S. Seo, J. Y. Park, and Y. Kim acknowledge the support from NRF (2022R1A2C1003006 and 2022R1A5A1085103). The authors thank the operators of the seismographic networks who provided waveform data: Korea Meteorological Administration and Korea Institute of Geoscience and Mineral Resources in Korea and National Research Institute for Earth Science and Disaster Prevention in Japan.

## References

- Abercrombie, R. E. (2015). Investigating uncertainties in empirical Green's function analysis of earthquake source parameters. *Journal of Geophysical Research: Solid Earth*, 120(6), 4263–4277. <https://doi.org/10.1002/2015JB011984>
- Abercrombie, R. E., Poli, P., & Bannister, S. (2017). Earthquake directivity, orientation, and stress drop within the subducting plate at the Hikurangi margin, New Zealand. *Journal of Geophysical Research: Solid Earth*, 122(12), 10–176. <https://doi.org/10.1002/2017JB014935>
- Andrews, D. J. (1980). A stochastic fault model: 1. Static case. *Journal of Geophysical Research*, 85(B7), 3867–3877. <https://doi.org/10.1029/JB085iB07p03867>
- Beroza, G. C., & Ellsworth, W. L. (1996). Properties of the seismic nucleation phase. *Tectonophysics*, 261(1–3), 209–227. [https://doi.org/10.1016/0040-1951\(96\)00067-4](https://doi.org/10.1016/0040-1951(96)00067-4)
- Bertero, M., Bindi, D., Boccacci, P., Cattaneo, M., Eva, C., & Lanza, V. (1997). Application of the projected Landweber method to the estimation of the source time function in seismology. *Inverse Problems*, 13(2), 465–486. <https://doi.org/10.1088/0266-5611/13/2/017>
- Campillo, M., Bouchon, M., & Massinon, B. (1984). Theoretical study of the excitation, spectral characteristics, and geometrical attenuation of regional seismic phases. *Bulletin of the Seismological Society of America*, 74(1), 79–90. <https://doi.org/10.1785/BSSA0740010079>
- Caswell, T. A., Droettboom, M., Lee, A., Hunter, J., Sales de Andrade, E., Firing, E., et al. (2020). matplotlib/matplotlib: REL: v3.3.2 (v3.3.2) [Software]. Zenodo. <https://doi.org/10.5281/zenodo.4030140>
- Dreger, D., Nadeau, R. M., & Chung, A. (2007). Repeating earthquake finite source models: Strong asperities revealed on the San Andreas Fault. *Geophysical Research Letters*, 34(23). <https://doi.org/10.1029/2007GL031353>
- Ellsworth, W. L., & Beroza, G. C. (1995). Seismic evidence for an earthquake nucleation phase. *Science*, 268(5212), 851–855. <https://doi.org/10.1126/science.268.5212.851>
- Ellsworth, W. L., & Beroza, G. C. (1998). Observation of the seismic nucleation phase in the Ridgecrest, California, earthquake sequence. *Geophysical Research Letters*, 25(3), 401–404. <https://doi.org/10.1029/97GL53700>
- Ellsworth, W. L., & Bulut, F. (2018). Nucleation of the 1999 Izmit earthquake by a triggered cascade of foreshocks. *Nature Geoscience*, 11(7), 531–535. <https://doi.org/10.1038/s41561-018-0145-1>
- Eshelby, J. D. (1957). The determination of the elastic field of an ellipsoidal inclusion, and related problems. *Proceedings of the royal society of London. Series A. Mathematical and physical sciences*, 241(1226), 376–396. <https://doi.org/10.1098/rspa.1957.0133>
- Gallegos, A., & Xie, J. (2020). A multichannel deconvolution method to retrieve source–time functions: Application to the regional Lg wave. *Geophysical Journal International*, 223(1), 323–347. <https://doi.org/10.1093/gji/ggaa303>
- Goldstein, P., & Snoke, A. (2005). "SAC availability for the IRIS Community", incorporated institutions for seismology data management Center electronic newsletter. (Version 101.6a). <https://www.osti.gov/biblio/875360>
- Harris, R. A. (2004). Numerical simulations of large earthquakes: Dynamic rupture propagation on heterogeneous faults. *Pure and Applied Geophysics*, 161(11–12), 2171–2181. <https://doi.org/10.1007/s00024-004-2556-8>
- Hartzell, S. H. (1978). Earthquake aftershocks as Green's functions. *Geophysical Research Letters*, 5(1), 1–4. <https://doi.org/10.1029/gl005i001p00001>
- Hunter, J. D. (2007). Matplotlib: A 2D graphics environment. *Computing in Science & Engineering*, 9(3), 90–95. <https://doi.org/10.1109/MCSE.2007.55>
- Jia, Z., Jin, Z., Marchandon, M., Ulrich, T., Gabriel, A. A., Fan, W., et al. (2023). The complex dynamics of the 2023 Kahramanmaraş, Turkey, Mw 7.8–7.7 earthquake doublet. *Science*, 381(6661), 985–990. <https://doi.org/10.1126/science.adi0685>
- Jia, Z., Zhan, Z., & Kanamori, H. (2022). The 2021 South Sandwich Island Mw 8.2 earthquake: A slow event sandwiched between regular ruptures. *Geophysical Research Letters*, 49(3), e2021GL097104. <https://doi.org/10.1029/2021GL097104>
- Kim, W.-Y. (1987). Modeling short-period crustal phases at regional distances for the seismic source parameter inversion. *Physics of the Earth and Planetary Interiors*, 47(2), 159–178. [https://doi.org/10.1016/0031-9201\(87\)90075-6](https://doi.org/10.1016/0031-9201(87)90075-6)
- Kim, W.-Y., Choi, H., & Noh, M. (2010). The 20 January 2007 Odaesan, Korea, earthquake sequence: Reactivation of a buried strike-slip fault? *Bulletin of the Seismological Society of America*, 100(3), 1120–1137. <https://doi.org/10.1785/0120090069>
- Kim, W.-Y., Park, J. Y., Seo, M.-S., Son, Y. O., Lim, H., Han, S., & Kim, Y. (2022). The 14 December 2021 Mw 4.9 Offshore Jeju Island, Korea, earthquake: Seismological observation of an intraplate earthquake provides insight into regional seismotectonics. *The Seismic Record*, 2(2), 107–117. <https://doi.org/10.1785/0320220012>
- Király-Proag, E., Satriano, C., Bernard, P., & Wiemer, S. (2019). Rupture process of the Mw 3.3 earthquake in the St. Gallen 2013 geothermal reservoir, Switzerland. *Geophysical Research Letters*, 46(14), 7990–7999. <https://doi.org/10.1029/2019gl082911>
- Lawson, C. L., & Hanson, R. J. (1974). *Solving least squares problems*. Prentice Hall.
- López-Comino, J. A., & Cesca, S. (2018). Source complexity of an injection induced event: The 2016 Mw 5.1 Fairview, Oklahoma earthquake. *Geophysical Research Letters*, 45(9), 4025–4032. <https://doi.org/10.1029/2018gl077631>
- Meng, H., & Fan, W. (2021). Immediate foreshocks indicating cascading rupture developments for 527 M 0.9 to 5.4 Ridgecrest earthquakes. *Geophysical Research Letters*, 48(19), e2021GL095704. <https://doi.org/10.1029/2021GL095704>
- Meng, Q., Ni, S., & Peng, Z. (2021). Complex source behaviors and spatiotemporal evolution of seismicity during the 2015–2016 earthquake sequence in Cushing, Oklahoma. *Journal of Geophysical Research: Solid Earth*, 126(6), e2021JB022168. <https://doi.org/10.1029/2021jb022168>
- Ohnaka, M. (1992). Earthquake source nucleation: A physical model for short-term precursors. *Tectonophysics*, 211(1–4), 149–178. [https://doi.org/10.1016/0040-1951\(92\)90057-D](https://doi.org/10.1016/0040-1951(92)90057-D)
- Pennington, C. N., Uchide, T., & Chen, X. (2022). Slip characteristics of induced earthquakes: Insights from the 2015 Mw 4.0 Guthrie, Oklahoma earthquake. *Journal of Geophysical Research: Solid Earth*, 127(5). <https://doi.org/10.1029/2021jb023564>
- Ripperger, J., Ampuero, J.-P., Mai, P. M., & Giardini, D. (2007). Earthquake source characteristics from dynamic rupture with constrained stochastic fault stress. *Journal of Geophysical Research*, 112(B4). <https://doi.org/10.1029/2006JB004515>
- Schimmel, M., & Paulsen, H. (1997). Noise reduction and detection of weak, coherent signals through phase-weighted stacks. *Geophysical Journal International*, 130(2), 497–505. <https://doi.org/10.1111/j.1365-246x.1997.tb05664.x>

- Seo, M.-S., Kim, W.-Y., & Kim, Y. (2022). Rupture directivity of the 2021 ML 2.2 Gwangyang, Korea, microearthquake: Toward resolving high-resolution rupture process of a small earthquake. *The Seismic Record*, 2(4), 227–236. <https://doi.org/10.1785/0320220030>
- Shi, J., Kim, W.-Y., & Richards, P. G. (1996). Variability of crustal attenuation in the northeastern United States from Lg waves. *Journal of Geophysical Research*, 101(B11), 25231–25242. <https://doi.org/10.1029/96JB02580>
- Stabile, T. A., Satriano, C., Orefice, A., Festa, G., & Zollo, A. (2012). Anatomy of a microearthquake sequence on an active normal fault. *Scientific Reports*, 2(1), 1–7. <https://doi.org/10.1038/srep00410>
- Stich, D., Martín, R., Morales, J., López-Comino, J. Á., & Mancilla, F. D. L. (2020). Slip partitioning in the 2016 Alboran Sea earthquake sequence (western mediterranean). *Frontiers in Earth Science*, 8, 587356. <https://doi.org/10.3389/feart.2020.587356>
- The ObsPy Development Team. (2022). ObsPy 1.3.0 (1.3.0) [Software]. Zenodo. <https://doi.org/10.5281/zenodo.6327346>
- Tian, D., & Kriegerowski, M. (2021). seism/HinetPy: 0.6.8 (0.6.8) [Software]. Zenodo. <https://doi.org/10.5281/zenodo.4599566>
- Uieda, L., Tian, D., Leong, W. J., Jones, M., Schlitzer, W., Grund, M., et al. (2022). PyGMT: A Python interface for the Generic Mapping Tools (v0.7.0) [Software]. Zenodo. <https://doi.org/10.5281/zenodo.6702566>
- Vallée, M. (2004). Stabilizing the empirical Green function analysis: Development of the projected Landweber method. *Bulletin of the Seismological Society of America*, 94(2), 394–409. <https://doi.org/10.1785/0120030017>
- Wessel, P., Luis, J. F., Uieda, L., Scharroo, R., Wobbe, F., Smith, W. H., & Tian, D. (2019). The generic mapping tools version 6. *Geochemistry, Geophysics, Geosystems*, 20(11), 5556–5564. <https://doi.org/10.1029/2019GC008515>
- Wu, Q., Chen, X., & Abercrombie, R. E. (2019). Source complexity of the 2015 Mw 4.0 Guthrie, Oklahoma earthquake. *Geophysical Research Letters*, 46(9), 4674–4684. <https://doi.org/10.1029/2019gl082690>
- Yoon, C. E., Yoshimitsu, N., Ellsworth, W. L., & Beroza, G. C. (2019). Foreshocks and mainshock nucleation of the 1999 Mw 7.1 Hector Mine, California, Earthquake. *Journal of Geophysical Research: Solid Earth*, 124(2), 1569–1582. <https://doi.org/10.1029/2018JB016383>